Nuclear Engineering and Technology 54 (2022) 3478–3487

Contents lists available at ScienceDirect

Nuclear Engineering and Technology

journal homepage: www.elsevier.com/locate/net

Original Article

Incorporation of anisotropic scattering into the method of characteristics

Anisur Rahman, Deokjung Lee*

Department of Nuclear Engineering, Ulsan National Institute of Science and Technology, 50 UNIST-gil, Ulsan, 44919, Republic of Korea

ARTICLE INFO

Article history:
Received 30 August 2021
Received in revised form
28 March 2022
Accepted 29 March 2022
Available online 31 March 2022

Keywords:
Neutron transport
Method of characteristics
Spherical harmonics
Legendre functions

ABSTRACT

In this study, we incorporate an anisotropic scattering scheme involving spherical harmonics into the method of characteristics (MOC). The neutron transport solution in a light water reactor can be significantly improved because of the impact of an anisotropic scattering source with the MOC flat source approximation. Several problems are selected to verify the proposed scheme and investigate its effects and accuracy. The MOC anisotropic scattering source is based on the expansion of spherical harmonics with Legendre polynomial functions. The angular flux, scattering source, and cross section are expanded in terms of the surface spherical harmonics. Later, the polynomial is expanded to achieve the odd and even parity of the source components. Ultimately, the MOC angular and scalar fluxes are calculated from a combination of two sources. This paper presents various numerical examples that represent the hot and cold conditions of a reactor core with boron concentration, burnable absorbers, and control rod materials, with and without a reflector or baffle. Moreover, a small critical core problem is considered which involves significant neutron leakage at room temperature. We demonstrate that an anisotropic scattering source significantly improves solution accuracy for the small core high-leakage problem, as well as for practical large core analyses.

1. Introduction

The solution of the neutron transport equation using the method of characteristics (MOC) is widely used for nuclear reactor core analysis. A three-dimensional (3-D) neutron transport code called STREAM [1], based on the MOC was developed for light water reactor neutronics analysis. Several methods have been used for the neutronics analysis of a reactor core. The conventional two-step method [2] (transport/diffusion based), the coarse mesh diffusion theory is used in whole core analysis whereas the fine-mesh neutron transport method is applied for fuel assembly. The Monte Carlo continuous-energy neutron transport simulation code [3,4] and the MOC based neutron transport code are also used worldwide. Transport-corrected cross sections with the MOC are usually used and numerous methods [5] are applied to correct the total cross section. Precise modeling of the core geometry for reactor analysis is difficult because the core geometry in the radial direction is complicated compared to the axial direction [2]. Therefore, a more realistic geometric discretization is necessary to acquire the outcomes. Explicit 3-D transport analysis can eliminate many approximations compared to the two-step method, although transport/diffusion-based method requires less time.

The earliest reactor analysis code based on the MOC was CACTUS [6]. This code was developed by the UK Atomic Energy Authority, but it was not widely used at the time because of the required processor speeds and higher memory requirements. However, the currently available computer capabilities have enabled the widespread use of the transport model for nuclear reactor neutronics analysis. This model permits an explicit representation of the geometry and provides reasonably accurate results. Time, energy, and space-dependent Boltzmann neutron transport equations are used in the transport model. In the MOC, the multidimensional partial differential equation is rewritten as an ordinary differential equation along a characteristic curve. Although flat source approximation is more widely used than other methods because of its simplicity, linear and quadratic neutron source approximations allow larger meshes compared to flat sources. Many codes, including DECART [7], nTRACER [8], MPACT [9], STREAM [1], PROTEUS-MOC [10], and OpenMOC [11], were developed based on the MOC. The 2-D/1-D method was originally developed and implemented in DECART [7]; it is solved the radial plane by the 2-D

* Corresponding author.
E-mail addresses: anisur@unist.ac.kr (A. Rahman), deokjung@unist.ac.kr (D. Lee).

https://doi.org/10.1016/j.net.2022.03.041

MOC, and the axial plane is solved by the SP3 or diffusion method. Later, nTRACER [8], MPACT [9], and PROTEUS-MOC [10] also adopted the 2-D/1-D method. Upgrading of the 2-D/1-D method [12–14] to address its limitations is still an ongoing process. OpenMOC solves the direct 3-D MOC transport equation, but it requires considerable memory and runtime. In contrast, the 3-D method of characteristics/diamond-difference method has been implemented in the neutron transport code STREAM, but it does not include any axial solvers.

Many solution schemes, including discrete ordinate (S_N), spherical harmonics (P_N), Monte Carlo, collision probability, and MOCs [15] have been developed in recent decades to solve the multi-group neutron transport equation. The development of the last two advanced reactor design methods is important because of the transport approximation. The spherical harmonics allow the strong anisotropic scatter areas to be easily used [16,17]. The orthonormal property of spherical harmonics enables expansion by the Legendre polynomial of degree ℓ, which is valid for both real and complex harmonics.

The coarse mesh finite difference (CMFD) acceleration method, which is based on the nodal diffusion equation, is used to accelerate the MOC transport solution in STREAM [1]. The 3-D MOC with pin-wise CMFD acceleration reduces the effective number of iterations and computing time. A 72-groups cross section library is used in the MOC whereas 8-groups is used for CMFD. In the CMFD solver, the assembly-wise solver is used to accelerate the pin-wise CMFD.

The purpose of this work is to evaluate the performance of anisotropic scattering and adopt more features in STREAM that could provide more realistic and accurate results. All simulations in this study were tested up to order 3. The MOC flat source approximation with a higher-order anisotropic scattering source scheme might be capable of improving the solution accuracy with respect to the reference.

2. Methodology

The neutron transport equation in the MOC can be written as a combination of 2-D radial (x, y) and 1-D axial components. The angular flux, scalar flux, and source are written with radial and axial parts, as follows:

$$\begin{aligned}\psi^{g}_{i,j,k}(s,z) &\approx \psi^{g}_{i,j,k}(s)b(z)\\ \phi^{g}(s,z) &\approx \overline{\phi}^{g}(s)b(z)\\ Q^{g}_{i,j}(s,z) &\approx \overline{Q}^{g}_{i,j,m}(s)b(z)\end{aligned} \tag{1}$$

where z is the axial direction coordinate, s is the radial x-y plane coordinate, i is the index of the azimuthal angle, j is the index of the polar angle, k is the index for the MOC ray segment, g is the index of the energy group, and m is the index for the source region.

The components of the angular flux, scalar flux, and source are written in any axial plane with linear interpolation of the upper and lower domains. Thus:

$$\begin{cases}\psi^{g}_{i,j,k}(s)b(z) = \psi^{g,0}_{i,j,k}(s) + \dfrac{z}{\Delta z}\left(\psi^{g,+}_{i,j,k}(s) - \psi^{g,-}_{i,j,k}(s)\right)\\ \overline{\phi}^{g}(s)b(z) = \overline{\phi}^{g,0}(s) + \dfrac{z}{\Delta z}\left(\overline{\phi}^{g,+}(s) - \overline{\phi}^{g,-}(s)\right) \qquad \dfrac{-\Delta z}{2} \le z \le \dfrac{\Delta z}{2}\\ \overline{Q}^{g}_{i,j,m}(s)b(z) = \overline{Q}^{g,0}_{i,j,m}(s) + \dfrac{z}{\Delta z}\left(\overline{Q}^{g,+}_{i,j,m}(s) - \overline{Q}^{g,-}_{i,j,m}(s)\right)\end{cases} \tag{2}$$

where z^0, z^+, and z^- are active, upper, and lower regions of the axial plane, respectively. The average value is defined as follows:

$$\begin{cases}\psi^{g,0}_{i,j,k}(s) = \dfrac{1}{2}\left(\psi^{g,+}_{i,j,k}(s) + \psi^{g,-}_{i,j,k}(s)\right)\\ \overline{\phi}^{g,0}_{m} = \dfrac{1}{2}\left(\overline{\phi}^{g,+}_{m} + \overline{\phi}^{g,-}_{m}\right)\\ \overline{Q}^{g,0}_{i,j,m} = \dfrac{1}{2}\left(\overline{Q}^{g,+}_{i,j,m} + \overline{Q}^{g,-}_{i,j,m}\right)\end{cases} \tag{3}$$

The steady-state 3-D neutron transport equation [1,18] along the characteristic line is

$$\cos\overline{\theta}_j \frac{\partial\psi^{g}_{i,j,k}(s,z)}{\partial s} + \sin\overline{\theta}_j \frac{\partial\psi^{g}_{i,j,k}(s,z)}{\partial z} + \sigma^{g}_{t,m}\psi^{g}_{i,j,k}(s,z) = Q^{g}_{i,j}(s,z) \tag{4}$$

where $\sigma^{g}_{t,m}$ is the total cross section at the flat source region m. The sine and cosine components indicate the axial and x-y planes.

By inserting the flux and source element from the approximation equations (1)–(3) into equation (4), the transport equation is

$$\begin{aligned}&\cos\overline{\theta}_j \frac{\partial\psi^{g}_{i,j,k}(s)b(z)}{\partial s} + \sin\overline{\theta}_j \frac{\partial\psi^{g}_{i,j,k}(s)b(z)}{\partial z} + \sigma^{g}_{t,m}\psi^{g}_{i,j,k}(s)b(z)\\ &= \overline{Q}^{g}_{i,j,m}b(z).\end{aligned} \tag{5}$$

Integrating equation (5) over the axial domain and dividing by the axial size (Δz) of the domain yields,

$$\cos\overline{\theta}_j \frac{\partial\psi^{g,0}_{i,j,k}(s)}{\partial s} + \frac{\sin\overline{\theta}_j}{\Delta z}\left(\psi^{g,+}_{i,j,k}(s) - \psi^{g,-}_{i,j,k}(s)\right) + \sigma^{g}_{t,m}\psi^{g,0}_{i,j,k}(s) = \overline{Q}^{g,0}_{i,j,m} \tag{6}$$

where the source is the sum of the fission and scattering source defined as follows:

$$\overline{Q}^{g,0}_{i,j,m} = \frac{1}{4\pi}\left(\frac{\chi^{g}_{m}}{k_{eff}}\sum_{g'}\nu\sigma^{g'}_{f,m}\overline{\phi}^{g',0}_{m} + \sum_{g'}\sigma^{g'\to g}_{s,m}\overline{\phi}^{g',0}_{m}\right). \tag{7}$$

Rewrite equation (6) by adding the term $\frac{2\sin\overline{\theta}_j}{\Delta z}\psi^{g,-}_{i,j,k}(s)$ on both sides

$$\begin{aligned}&\cos\overline{\theta}_j \frac{\partial\psi^{g,0}_{i,j,k}(s)}{\partial s} + \frac{2\sin\overline{\theta}_j}{\Delta z}\psi^{g,0}_{i,j,k}(s) + \sigma^{g}_{t,m}\psi^{g,0}_{i,j,k}(s)\\ &= \overline{Q}^{g,0}_{i,j,m} + \frac{2\sin\overline{\theta}_j}{\Delta z}\psi^{g,-}_{i,j,k}(s).\end{aligned} \tag{8}$$

The term $\frac{2\sin\overline{\theta}_j}{\Delta z}\psi^{g,-}_{i,j,k}(s)$ on the right-side acts as a surface source from the bottom plane, which merges with the fission and scattering sources.

$$\frac{2\sin\overline{\theta}_j}{\Delta z}\psi^{g,-}_{i,j,k}(s) \approx \frac{2\sin\overline{\theta}_j}{\Delta z}\bar{\bar{\psi}}^{g,-}_{i,j,m}(s) \tag{9}$$

where $\bar{\bar{\psi}}^{g,-}_{i,j,m}(s)$ is the average angular flux of the region.

Finally, the general form of the transport equation is

$$\cos\overline{\theta}_j \frac{\partial\psi^{g,0}_{i,j,k}(s)}{\partial s} + \tilde{\sigma}^{g}_{t,m}\psi^{g,0}_{i,j,k}(s) = \overline{S}^{g,0}_{i,j,m} \tag{10}$$

where $\tilde{\sigma}^{g}_{t,m}$ is the modified total cross section and is defined by

$$\tilde{\sigma}^{g}_{t,m} = \sigma^{g}_{t,m} + \frac{2\sin\bar{\theta}_j}{\Delta z}. \tag{11}$$

Total source is defined by

$$\bar{S}^{g,0}_{i,j,m} = \bar{Q}^{g,0}_{i,j,m} + \frac{2\sin\bar{\theta}_j}{\Delta z}\bar{\psi}^{g,-}_{i,j,m}(s). \tag{12}$$

The analytical solution of equation (10) is

$$\psi^{g,0}_{out,i,j,k} = \psi^{g,0}_{in,i,j,k} e^{-\tilde{\sigma}^{g}_{t,m} t'_{i,j,k}} + \frac{\bar{S}^{g}_{i,j,m}}{\tilde{\sigma}^{g}_{t,m}}\left(1 - e^{-\tilde{\sigma}^{g}_{t,m} t'_{i,j,k}}\right), \tag{13}$$

where $\psi^{g,0}_{out,i,j,k}$ is the outgoing angular flux from the ray segment, $\psi^{g,0}_{in,i,j,k}$ is the incoming angular flux to the segment, $t_{i,j,k}$ is the length of the segment projected on x-y plane, and $t'_{i,j,k}$ is the actual segment length.

The average angular flux of any track is defined by

$$\begin{aligned}\bar{\psi}^{g,0}_{i,j,k} &= \frac{\int_0^{t'_{i,j,k}} \psi^{g,0}_{i,j,k}(s)ds}{\int_0^{t'_{i,j,k}} ds} = \frac{\int_0^{t'_{i,j,k}} \left\{\psi^{g,0}_{i,j,k}(0)e^{-\tilde{\sigma}^{g}_{t,m}s} + \frac{\bar{S}^{g}_{i,j,m}}{\tilde{\sigma}^{g}_{t,m}}\left(1 - e^{-\tilde{\sigma}^{g}_{t,m}s}\right)\right\} ds}{t'_{i,j,k}} \\ &= \frac{\bar{S}^{g}_{i,j,m}}{\tilde{\sigma}^{g}_{t,m}} + \frac{1}{\tilde{\sigma}^{g}_{t,m} t'_{i,j,k}}\left(\psi^{g,0}_{in,i,j,k} - \frac{\bar{S}^{g}_{i,j,m}}{\tilde{\sigma}^{g}_{t,m}}\right)\left(1 - e^{-\tilde{\sigma}^{g}_{t,m} t'_{i,j,k}}\right).\end{aligned} \tag{14}$$

The average angular flux in any region defined by

$$\begin{aligned}\bar{\bar{\psi}}^{g,0}_{i,j,m} &= \frac{\sum_{k\in m} \bar{\psi}^{g,0}_{i,j,k} t'_{i,j,k} d_i}{\sum_{k\in m} t'_{i,j,k} d_i} \\ &= \sum_{k\in m}\left[\frac{\bar{S}^{g}_{i,j,m}}{\tilde{\sigma}^{g}_{t,m}} + \frac{d_i \cos\theta_j}{\tilde{\sigma}^{g}_{t,m} A_m}\left(\frac{\bar{S}^{g}_{i,j,m}}{\tilde{\sigma}^{g}_{t,m}} - \psi^{g,0}_{in,\,i,j,k}\right)\left(1 - e^{-\tilde{\sigma}^{g}_{t,m} t'_{i,j,k}}\right)\right].\end{aligned} \tag{15}$$

where d_i is the ray spacing, and A_m is the analytic area of the flat source region m.

The region-wise scalar flux (each flat source) is calculated as

$$\phi^{g,0}_{m} = 4\pi \sum_j \sum_i \bar{\bar{\psi}}^{g,0}_{i,j,m} \omega_i \omega_j, \tag{16}$$

where ω_i and ω_j are the weights for the azimuthal and polar angles, respectively.

The Legendre polynomials [19] were applied to enlarge the angle dependent on the scattering cross sections. The scattering source is a combination of incoming and outgoing flight directions or the cosine of the angle between them, and it can be expanded in terms of the scattering angle:

$$\sigma_s(r, E' \to E, \mu) = \frac{1}{4\pi}\sum_{l=0}^{N}(2l+1)\sigma^{l}_{s}(r, E', \omega'.\omega)P_l(\mu). \tag{17}$$

From equation (7), the total source is the sum of the fission and scattering sources. The scattering source term is defined as follows:

$$Q_s(r, E, \omega) = \int_0^{\infty} dE' \int_0^{4\pi} d\Omega'[\sigma_s(r, E' \to E, \omega'.\omega)\psi(r, E', \omega')]. \tag{18}$$

The normalized spherical harmonics functions $Y_{l,m}(\omega)$ are defined by

$$Y_{l,m}(\omega) = \sqrt{\frac{(2l+1)}{4\pi}}\sqrt{\frac{(l-m)!}{(l+m)!}}P^{m}_{l}(\mu)e^{im\phi}, 0 \le |m| \le l \le \infty, \tag{19}$$

where $P^{m}_{l}(\mu)$ is the associated Legendre function, and μ and ϕ are the cosines of the polar and azimuthal angle of the direction of vector Ω, respectively.

$$P^{m}_{l}(\mu) = \left\{\begin{array}{ll}(-1)^m\left(1-\mu^2\right)^{\frac{m}{2}}\left(\frac{d}{d\mu}\right)^m P_l(\mu) & m \ge 0 \\ (-1)^m\left(\frac{(l-|m|)!}{(l+|m|)!}\right)P^{|m|}_{l}(\mu) & m < 0\end{array}\right\} \tag{20}$$

The modified scattering source term, equation (18), is now

$$\begin{aligned}Q_s(r, E, \omega) &= \int_0^{\infty} dE'\left[\sum_{l=0}^{N}\sigma^{l}_{s}(r, E' \to E, \omega'.\omega)\sum_{m=-l}^{l}\psi_{l,m}(r, E', \omega')Y_{l,m}(\omega)\right] \\ &= \int_0^{\infty} dE'\left[\sum_{l=0}^{N}\sigma^{l}_{s}(r, E' \to E, \omega'.\omega)\left\{\psi_{l,0}(r, E', \omega')Y_{l,0}(\omega)\right.\right. \\ &\left.\left. + \sum_{m=1}^{l}\left(\psi_{l.m}(r, E', \omega')Y_{l,m}(\omega) + \psi^{*}_{l,m}(r, E', \omega')Y^{*}_{l.m}(\omega)\right)\right\}\right].\end{aligned} \tag{21}$$

By identifying the real and imaginary part of each component then we can write,

$$\begin{aligned}Q_s(r, E, \omega) &= \int_0^{\infty} dE'\left[\sum_{l=0}^{N}\sigma^{1}_{s}(r, E' \to E, \omega'.\omega)\right. \\ &\left\{\psi_{l.0}(r, E', \omega')Y_{l,0}(\omega) + 2\sum_{m=1}^{l}\left(\psi_{l.m(Re)}(r, E', \omega')Y_{l,m(Re)}(\omega)\right.\right. \\ &\left.\left. + \psi_{l.m(Im)}(r, E', \omega')Y_{l.m(Im)}(\omega)\right)\right\}\Bigg].\end{aligned} \tag{22}$$

More simply,

$$\begin{aligned}Q_s(r, E, \omega) = &\int_0^{\infty} dE'\left[\sum_{l=0}^{N}\sigma^{1}_{s}(r, E' \to E, \omega'.\omega)\right. \\ &\left.\sum_{m=-l}^{l}R_{l,m}(\omega)\psi_{l.m}(r, E', \omega')\right],\end{aligned} \tag{23}$$

where

$$R_{l,m}(\omega) = \left\{\begin{array}{ll}\sqrt{\frac{(2l+1)}{4\pi}}\sqrt{2\frac{(l-m)!}{(l+m)!}}P^{m}_{l}(\mu)\cos(m\phi) & m > 0 \\ \sqrt{\frac{(2l+1)}{4\pi}}P_l(\mu) & m = 0 \\ \sqrt{\frac{(2l+1)}{4\pi}}\sqrt{2\frac{(l-|m|)!}{(l+|m|)!}}P^{|m|}_{l}(\mu)\sin(|m|\phi) & m < 0\end{array}\right\}$$

and the angular flux (P_N flux) moments are defined by

$$\phi_{l,m}(r, E') = \int_0^{4\pi} d\Omega' R_{l,m}(\omega)\psi_{l,m}(r, E', \omega'), \quad (24)$$

where $R_{l,m}(\omega')$ is part of the spherical harmonics.

3. Verification

All the studies were performed with the MOC ray spacing of 0.05 cm, 48 azimuthal angles, and 6 polar angles. The black boundary was applied at the top and bottom in the 3-D problem, and the boundary conditions at the other sides depended on the problem. The mesh for each pin cell consisted of five radial rings for the inner zone, and three radial rings for the outer zone. In 3-D, 170 and 64 axial planes were used in the VERA and Babcock & Wilcox (B&W) problems, respectively. Transport-corrected (PCP0) results and results that are not transport-corrected (P0) were added to each problem to realize a comparative study.

3.1. Two-dimensional problem

3.1.1. Single lattice

A pressurized water reactor fuel assembly (Westinghouse designed) was selected to test the accuracy of the anisotropic scattering source scheme and compare it to Monte Carlo reference. The assembly consisted of a 17 × 17 fuel array with 264 fuel rods, 24 guide tubes, and one instrument tube. The geometry and number of the flat source regions of the fuel pin are shown in Fig. 1. A summary of the assembly parameters is presented in Table 1. Detailed technical specifications and reference solutions were obtained from the VERA core physics benchmark progression problem [20]. The fuel and cladding material were 3.1 wt% UO_2 and Zircaloy-4, respectively. Identical temperatures were used for all regions [20].

The results in Table 2 demonstrate the situation of the lattice in a typical reactor startup and at full power operation in unrodded and rodded conditions, including different burnable poisons. The temperature range of the fuel is commonly observed under hot zero power (HZP) or full power reactor operation. It is common to observe a higher error when an anisotropic scattering source is not used. On the other hand, the eigenvalue differences are below 100 pcm when using scattering source order 3, except 2C (−164 pcm), 2D (−277 pcm), and 2 N (−144 pcm). Furthermore, lower pin power differences were observed in order 3 compared to that in P0.

3.1.2. B&W simple experiments

The Babcock & Wilcox (B&W) [21] series 1484 core I and II experiments consisted of two very simple cores (one circular and one square), as shown in Fig. 2. These two cores were not

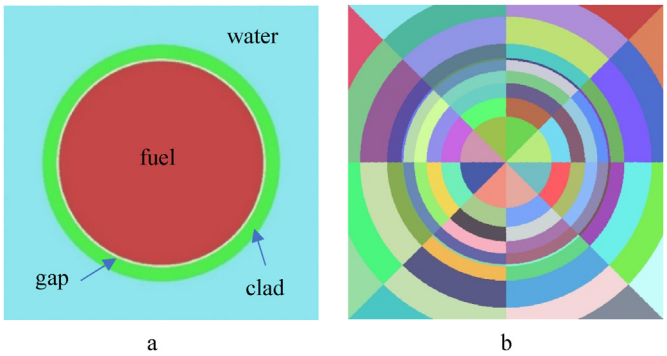

Fig. 1. Geometry of single pin (a) Materials, and (b) Flat source regions.

Table 1
Specification of fuel assembly.

Input	Value
Pellet radius	0.4096 cm
Inner clad radius	0.4180 cm
Outer clad radius	0.4750 cm
Rod pitch	1.26 cm
Assembly pitch	21.50 cm
Pellet material	UO_2 (3.1% w/o U235)
Clad material	Zircaloy-4
Fill gas material	Helium

Table 2
Summary results of a single lattice.

Problem	PN order	k-effective		Pin Power Distribution diff.[b]	
		calculated	diff.(pcm)[a]	PW.(%)	Max.(%)
2A	P3	1.18217	−0.5	0.20	−0.36
	P0[c]	1.18114	−103	0.24	0.60
	TCP0[d]	1.18164	−53	0.20	−0.36
2B	P3	1.18292	−44	0.14	−0.26
	P0	1.18216	−120	0.27	0.63
	TCP0	1.18253	−83	0.17	−0.36
2C	P3	1.17221	−164	0.09	0.21
	P0	1.17141	−234	0.26	0.64
	TCP0	1.17159	−216	0.11	−0.25
2D	P3	1.16282	−277	0.08	0.18
	P0	1.16210	−349	0.27	0.63
	TCP0	1.16230	−329	0.10	−0.23
2E	P3	1.06916	−46	0.13	0.23
	P0	1.07304	341	0.65	1.18
	TCP0	1.06936	−26	0.13	0.25
2F	P3	0.97554	−47	0.07	0.14
	P0	0.98221	619	1.05	2.03
	TCP0	0.97606	4	0.11	−0.28
2G	P3	0.84820	50	0.13	0.24
	P0	0.86413	1643	1.98	3.53
	TCP0	0.85038	268	0.17	0.50
2H	P3	0.78733	−89	0.16	0.26
	P0	0.80855	2032	2.77	4.85
	TCP0	0.79051	228	0.19	0.55
2I	P3	1.17970	−21	0.14	0.19
	P0	1.17869	−122	0.29	0.71
	TCP0	1.17914	−77	0.17	0.32
2J	P3	0.97466	−53	0.11	0.14
	P0	0.98130	610	1.07	2.21
	TCP0	0.97515	−4	0.11	−0.27
2K	P3	1.01915	−91	0.11	−0.35
	P0	1.02532	525	1.00	2.22
	TCP0	1.01958	−48	0.11	−0.27
2L	P3	1.01822	−69	0.24	−0.52
	P0	1.01823	−68	0.69	−1.59
	TCP0	1.01782	−109	0.30	−0.70
2 M	P3	0.93855	−24	0.28	−0.54
	P0	0.93789	−90	0.58	−1.22
	TCP0	0.93810	−69	0.36	−0.67
2 N	P3	0.86836	−144	0.15	−0.33
	P0	0.87401	502	1.66	−2.77
	TCP0	0.86854	−123	0.25	−0.49
2O	P3	1.04728	−44	0.15	0.44
	P0	1.05290	517	0.47	−2.50
	TCP0	1.04710	−62	0.16	0.37
2P	P3	0.92699	−42	0.18	0.37
	P0	0.93625	884	0.51	−2.78
	TCP0	0.92754	13	0.20	−0.43
2Q	P3	1.17162	−32	0.20	−0.77
	P0	1.17079	−115	0.56	−1.11
	TCP0	1.17108	−86	0.21	−0.64

[a] Difference = $(k_{eff} - k_{eff}^{ref.}) \times 10^{5}$.
[b] Difference of pin power: PW.: power weight difference; Max.: maximum difference.
[c] Without transport correction.
[d] Transport corrected using the inflow method.

heterogeneous in any way (e.g., water holes, absorber holes, enrichment splits). Both cores had identical fuel pins and differed only in size and shape. Core I contained 458 pins (2.459 wt%) arranged in a circle whereas core II had 1764 fuel pins (2.459 wt%) arranged in a square. The configuration of core I shows a very high neutron leakage issue compared to that of core II. However, cores I and II offer a good indication of the accuracy of radial leakage and anisotropic scattering.

The B&W series 1484 core I and II results are shown in Tables 3 and 4, respectively. The core I eigenvalue difference at P0 was more than 10000 pcm. Inversely, the values compensate from 10426 pcm to −44 pcm and 8 pcm at P1 and P3, respectively. In contrast core II compensates 4184 pcm−284 pcm and 122 pcm at P1 and P3, respectively. The average root mean square (RMS) errors of cores I and II were 1.01 and 0.60, respectively at P1, whereas the average RMS errors of cores I and II were 0.49 and 0.16, respectively at P3. In contrast, the relative maximum pin power differences were 1.5% and 0.99%, respectively at P3. However, the pin power error increased from 1.5% to 10.73% and from 0.99% to 22.78% at P0.

3.1.3. 3 × 3 core (Colorset) and quarter core problems

A detailed description of these two problems is similar to the VERA problem [20]. The Colorset problem, as shown in Fig. 3, consists of 3 × 3 core at the beginning of life (BOL) and in HZP isothermal conditions. This problem also tests the rod cluster control assembly (RCCA) parameter (Silver−Indium−Cadmium control rods (AIC), and B_4C) ability in the assembly guide tubes. The loading pattern uses 2.11% and 2.619% enrichment with the center control rod assembly and run octant symmetry, respectively.

On the other hand, the quarter-core problem has a design similar to that of a commercial reactor. The fuel assembly, number of Pyrex rods (PY), and control rod configuration are shown in Fig. 4. This problem tests the ability of Pyrex, AIC, and B_4C absorbers in the assembly guide tubes and models the core baffle and other core structures.

Table 5 shows the Colorset problem results, showing three types of parameters. The difference in the effective multiplication factor for the three cases was below 100 pcm, and this difference was below 50 pcm at P2 and P3. The control rod worth and pin power distribution were in good agreement with reference [20].

Table 6 presents the results of the 2-D large-core analyses. The overall performances of P1, P2, and P3 with Pyrex, AIC, and B_4C absorbers were satisfactory. In the Pyrex case (5A), the maximum eigenvalue difference was −154 pcm, −104 pcm, and −110 pcm at P1, P2, and P3, respectively. However, in terms of the power difference, P1 was more precise than P2 and P3 (maximum 1.11% and 0.598% power weight difference (PWD)). On the other hand, the combined performance of Pyrex and control rod improves when the number of P_N orders increases in terms of the eigenvalue difference and pin power distribution. The eigenvalue difference

Table 3
Summary results of 2-D B&W 1484 core I.

PN order	k-effective	Reference	Diff. (pcm)	Pin Power Distribution diff.	
				PW.(%)	Max.(%)
P3	1.01568	1.01560	8	0.49	1.50
P2	1.01582	±0.000036	22	0.81	1.59
P1	1.01516		−44	1.01	2.09
P0	1.11986		10426	3.87	10.73
TCP0	1.01692		132	0.21	0.63

Table 4
Summary results of 2-D B&W 1484 core II.

PN order	k-effective	Reference	Diff. (pcm)	Pin Power Distribution diff.	
				PW.(%)	Max.(%)
P3	1.01714	1.01592	122	0.16	0.99
P2	1.01745	±0.000036	153	0.18	1.67
P1	1.01876		284	0.60	4.02
P0	1.05776		4184	3.20	22.78
TCP0	1.01582		−10	0.38	1.75

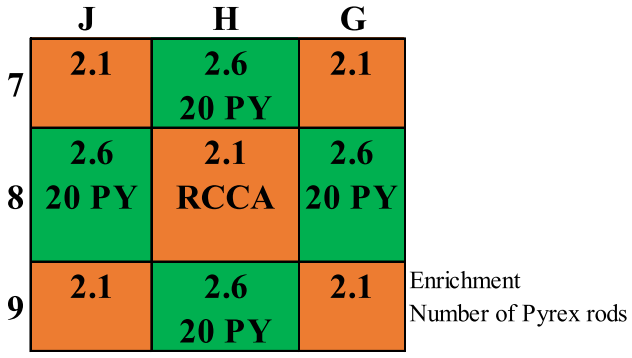

Fig. 3. 3 × 3 core assembly, poison, and control layout (Colorset).

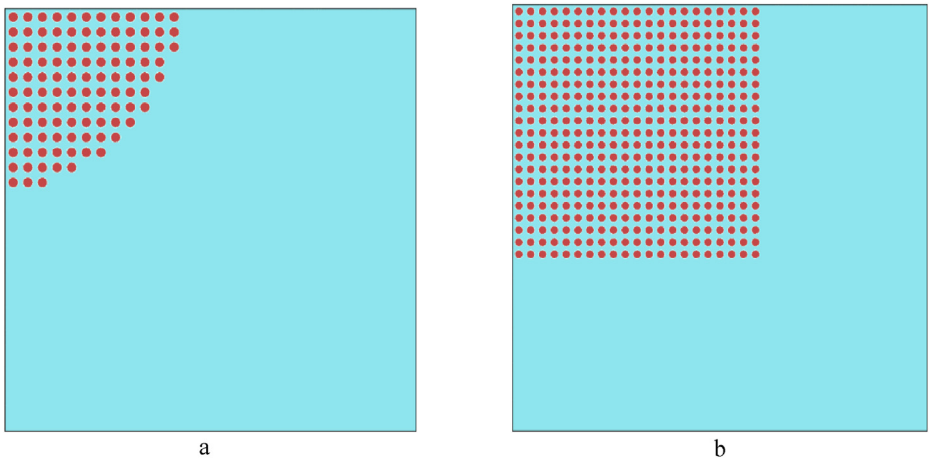

Fig. 2. Geometry (2-D) of B&W series 1484 (simple critical) (a) core I, and (b) core II.

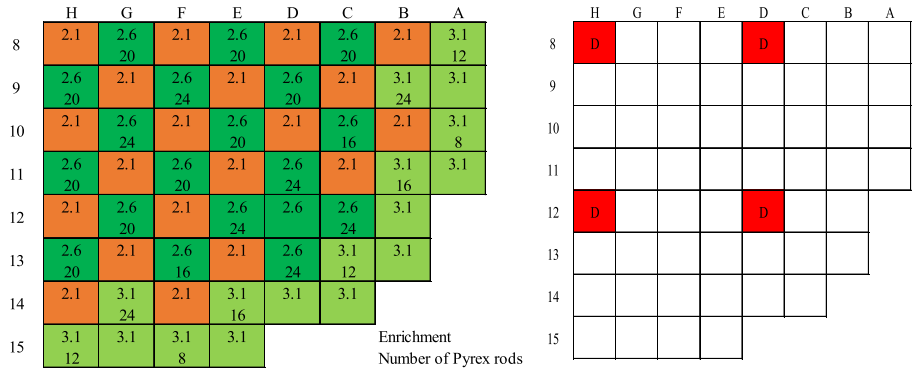

Fig. 4. Quarter core assembly: poison (left) and control rod layout (right).

Table 5
Results of 2-D 3 × 3 core (Colorset) analyses.

Problem	PN order	k-effective		Rod worth (pcm)		Pin power distribution diff.	
		calculated	diff.(pcm)	calculated	diff.	PW.(%)	Max.(%)
4A	P3	1.00982	−41	–	–	0.14	0.42
	P2	1.00979	−38	–	–	0.15	0.42
	P1	1.00949	−74	–	–	0.16	0.41
	P0	1.01332	308	–	–	2.40	4.88
	TCP0	1.00973	−50	–	–	0.17	0.55
4B	P3	0.98311	−33	2690	−7	0.15	0.46
	P2	0.98309	−29	2688	−9	0.16	0.46
	P1	0.98260	−85	2711	14	0.17	0.46
	P0	0.99200	855	2121	−576	6.68	−20.78
	TCP0	0.98317	−28	2675	−22	0.24	1.24
4C	P3	0.97990	−39	3023	−1	0.17	−0.76
	P2	0.97995	−34	3021	−3	0.19	−0.89
	P1	0.97932	−97	3052	28	0.23	−1.05
	P0	0.98996	967	2329	−695	7.23	−23.73
	TCP0	0.97997	−32	3008	−16	0.24	1.26

was below 100 pcm with the combination of Pyrex and the control rod (AIC or B_4C) at P2, and P3. However, the maximum power difference was in the range 0.92%–1.55% and 0.443%-0.492 PWD in the pin power distribution at P1, P2, and P3. A summary of the 2-D quarter-core calculation results at beginning of cycle is provided in Table 6, and a comparison of the fuel assembly (FA)-wise powers is shown in Figs. 5–7.

Table 6
Results of 2-D large quarter-core analyses.

Problem	PN order	k-effective		Assembly power diff.	
		calculated	diff.(pcm)	PW.(%)	Max.(%)
5A	P3	1.00298	−110	0.912	−1.60
	P2	1.00304	−104	0.924	−1.60
	P1	1.00254	−154	0.598	−1.11
	P0	1.01604	1195	44.44	103.01
	TCP0	1.00279	−129	0.704	1.39
5B	P3	0.99084	−65	0.450	−0.92
	P2	0.99091	−58	0.453	−0.94
	P1	0.99029	−120	0.443	−1.43
	P0	1.00870	1720	58.17	160.07
	TCP0	0.99061	−88	0.384	0.81
5C	P3	0.98953	−69	0.492	−1.11
	P2	0.98960	−62	0.492	−1.14
	P1	0.98896	−126	0.493	−1.55
	P0	1.00914	1891	59.57	166.64
	TCP0	0.98930	−92	0.382	0.76

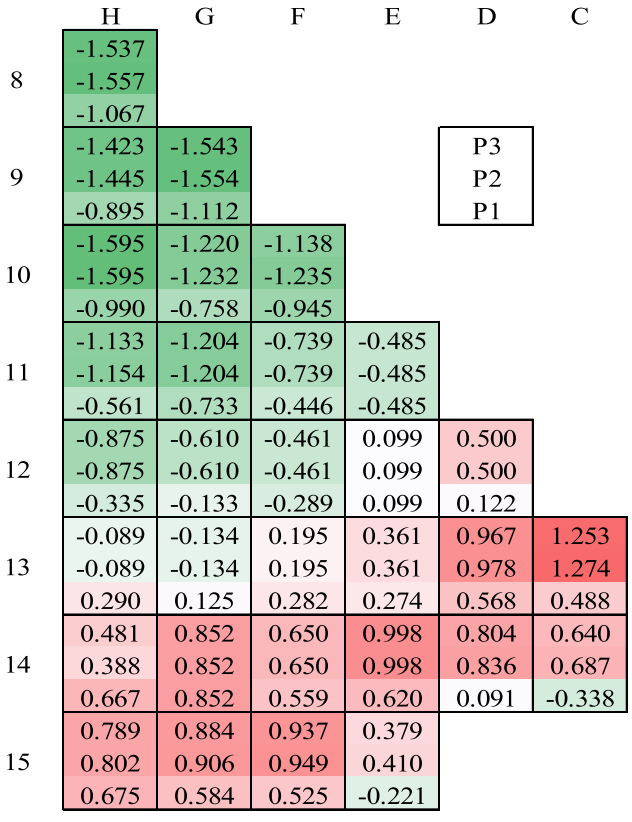

Fig. 5. Difference in assembly power distribution (Problem 5A, unit: %).

	H	G	F	E	D	C
	-0.814					
8	-0.837					
	-0.206					
	-0.553	-0.923			P3	
9	-0.580	-0.946			P2	
	0.037	-0.340			P1	
	-0.494	-0.435	-0.755			
10	-0.516	-0.459	-0.755			
	0.043	0.149	-0.270			
	-0.051	-0.392	-0.254	-0.567		
11	-0.063	-0.403	-0.254	-0.567		
	0.406	0.050	0.141	-0.193		
	0.125	0.037	-0.256	-0.113	-0.107	
12	0.107	0.027	-0.256	-0.113	-0.091	
	0.426	0.344	0.002	0.098	-0.124	
	0.430	0.076	0.159	-0.123	0.003	-0.133
13	0.430	0.076	0.159	-0.123	0.015	-0.097
	0.623	0.240	0.319	-0.123	-0.252	-0.748
	0.557	0.724	0.250	0.322	-0.208	-0.586
14	0.557	0.724	0.250	0.322	-0.178	-0.538
	0.480	0.568	0.097	-0.015	-0.829	-1.432
	0.776	0.557	0.458	-0.239		
15	0.776	0.557	0.458	-0.226		
	0.380	0.035	-0.051	-0.812		

Fig. 6. Difference in assembly power distribution (Problem 5B, unit: %).

	H	G	F	E	D	C
	-1.118					
8	-1.144					
	-0.659					
	-0.600	-0.889			P3	
9	-0.600	-0.900			P2	
	-0.044	-0.317			P1	
	-0.462	-0.385	-0.748			
10	-0.473	-0.408	-0.748			
	0.073	0.182	-0.163			
	-0.072	-0.395	-0.273	-0.517		
11	-0.084	-0.405	-0.273	-0.517		
	0.361	0.044	0.224	-0.138		
	-0.128	-0.011	-0.228	-0.147	-0.417	
12	-0.148	-0.022	-0.228	-0.157	-0.417	
	0.030	0.280	0.031	0.037	-0.579	
	0.468	0.135	0.209	-0.111	-0.130	-0.276
13	0.468	0.053	0.209	-0.111	-0.117	-0.253
	0.565	0.216	0.288	-0.111	-0.416	-0.923
	0.637	0.738	0.291	0.308	-0.301	-0.687
14	0.637	0.738	0.291	0.308	-0.271	-0.640
	0.561	0.661	0.141	0.059	-0.919	-1.550
	0.837	0.629	0.450	-0.216		
15	0.837	0.629	0.450	-0.191		
	0.454	0.208	0.061	-0.751		

Fig. 7. Difference in assembly power distribution (Problem 5C, unit: %).

3.2. Three-dimensional problem

3.2.1. VERA 3-D HZP Assembly

The three-dimensional single-assembly problem was taken from the VERA [20] specification. The geometry of the assembly consists of a Westinghouse 17 × 17 array with BOL and HZP conditions. The axial layout of the assembly is shown in Fig. 8. Problem 3A uses a boron concentration of 1300 ppm, 3.1% w/o enrichment of UO_2, and a temperature of 600 K, whereas problem 3B uses a boron concentration of 2250 ppm, 2.619% w/o enrichment of UO_2, and a temperature of 565 K. In addition to being close to critical 3B uses 16 Pyrex rods. The active fuel height of the assembly was 365.76 cm excluding the plate (5.0 cm), and nozzle (6.053 cm) at the bottom and the plenum (16.0 cm), nozzle (8.827 cm), and plate (6.6 cm) at the top.

Table 7 shows the results of the 3-D single assembly analyses. In all cases, the eigenvalue difference was less than 50 pcm, less than 1% of PWD, and nearly 2.50% maximum pin power difference in 3A.

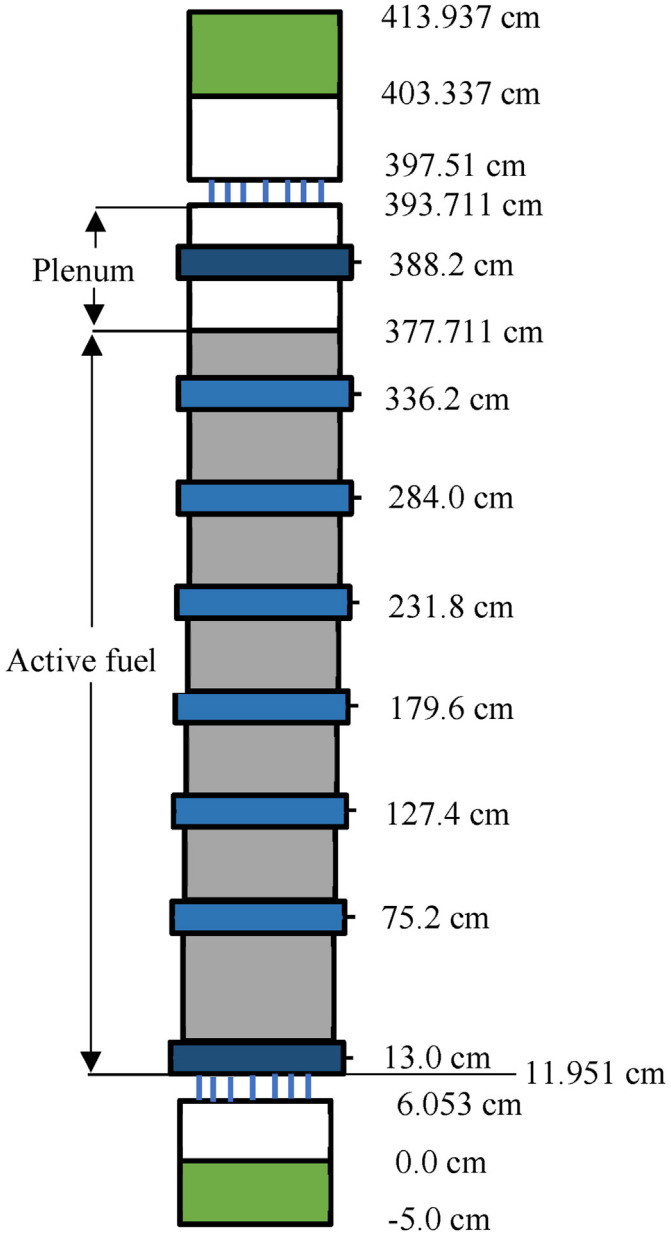

Fig. 8. Single assembly axial geometry [20].

Table 7
Summary of single assembly results.

Problem	PN order	k-effective		Pin Power Distribution diff.	
		calculated	diff.(pcm)	PW.(%)	Max.(%)
3A	P3	1.17562	−10	0.91	2.56
	P2	1.17551	−21	0.93	2.57
	P1	1.17539	−33	0.94	2.52
	P0	1.17427	−145	0.84	2.74
	TCP0	1.17319	−253	0.95	2.71
3B	P3	1.00072	57	0.791	2.10
	P2	1.00079	64	0.804	2.10
	P1	1.00019	5	0.794	2.10
	P0	1.00650	635	1.339	3.60
	TCP0	0.99970	−45	0.83	2.28

Table 8
Results of 3-D B&W cores I and II.

Problem	PN order	k-effective		Pin Power Distribution diff.	
		calculated	diff.(pcm)	PW.(%)	Max.(%)
1484 core I	P3	1.00015	89	0.73	1.83
	P2	1.00028	102	0.96	1.99
	P1	1.00591	665	1.17	2.48
	P0	1.10891	10965	4.71	11.56
	TCP0	1.00035	109	0.76	1.45
1484 core II	P3	1.00024	266	1.12	4.46
	P2	1.00025	267	1.12	4.46
	P1	1.00488	730	1.30	6.10
	P0	1.04560	4802	5.16	26.32
	TCP0	0.99935	177	0.98	3.10

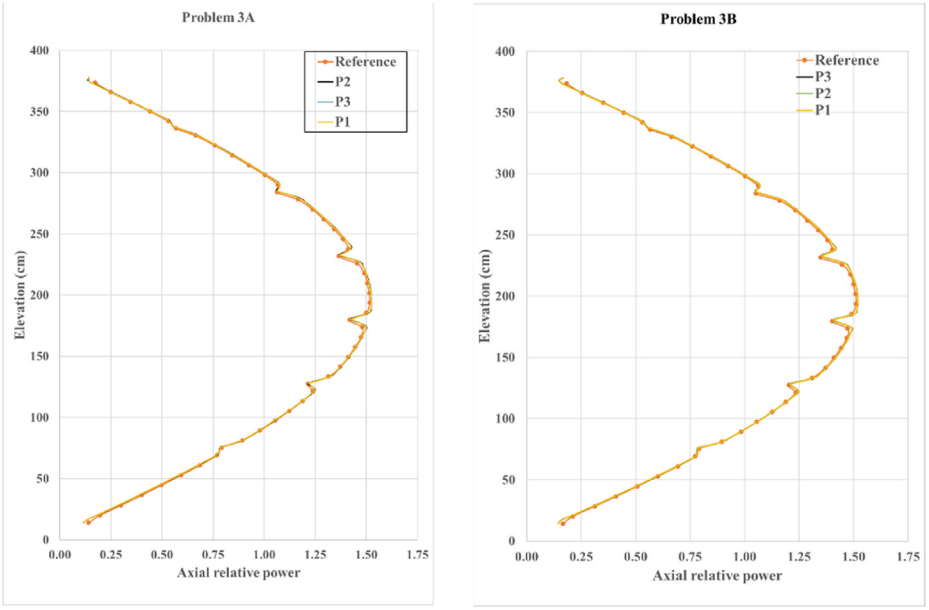

Fig. 9. Axial power distribution.

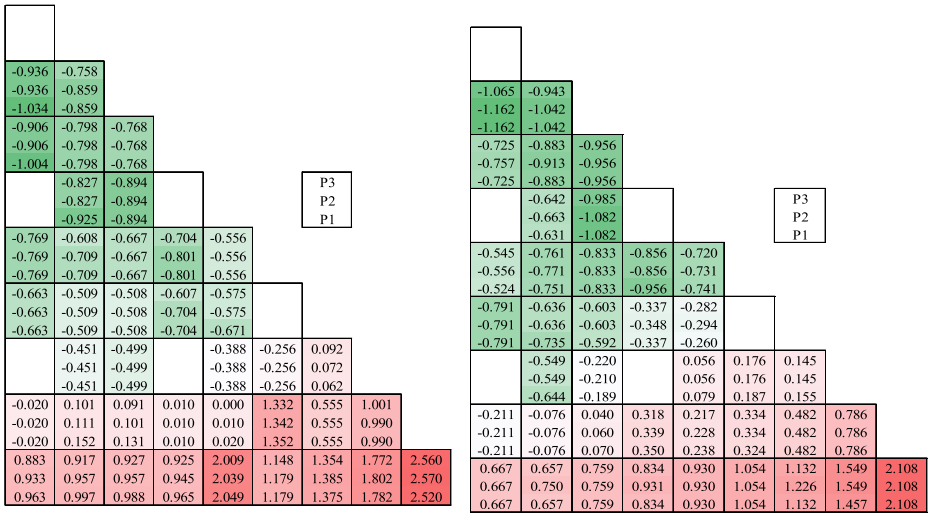

Fig. 10. Fuel radial pin power percent error distribution (a) 3A, and (b) 3B.

-0.760	-0.840	-0.697	-0.780	-0.640	-0.531	-0.504	-0.339	-0.058	0.457	1.198	1.837
-1.061	-1.069	-1.086	-1.102	-0.976	-0.798	-0.695	-0.578	-0.320	0.309	1.322	1.775
-1.212	-1.222	-1.164	-1.264	-1.145	-0.977	-0.887	-0.755	-0.468	0.236	1.458	2.226
-0.831	-0.845	-0.818	-0.784	-0.701	-0.569	-0.487	-0.341	-0.016	0.457	1.092	1.747
-1.060	-0.999	-1.054	-0.947	-0.871	-0.749	-0.584	-0.457	-0.096	0.506	1.422	1.999
-1.213	-1.076	-1.133	-1.029	-0.956	-0.930	-0.777	-0.625	-0.234	0.457	1.593	2.489
-0.842	-0.773	-0.772	-0.742	-0.741	-0.584	-0.407	-0.320	0.059	0.596	1.281	1.223
-1.076	-1.009	-0.932	-0.908	-0.915	-0.769	-0.605	-0.449	-0.022	0.694	1.689	1.315
-1.232	-1.088	-1.094	-1.075	-1.002	-0.954	-0.804	-0.610	-0.139	0.707	1.944	1.955
-0.748	-0.756	-0.715	-0.635	-0.617	-0.499	-0.410	-0.134	0.280	0.727	1.114	
-1.070	-0.918	-0.881	-0.807	-0.797	-0.691	-0.585	-0.256	0.256	0.956	1.623	
-1.151	-1.082	-1.048	-0.980	-0.978	-0.882	-0.760	-0.401	0.185	1.063	1.993	
-0.710	-0.712	-0.633	-0.594	-0.510	-0.449	-0.230	0.053	0.555	1.163	0.566	
-0.963	-0.882	-0.894	-0.774	-0.699	-0.549	-0.359	-0.028	0.627	1.493	1.108	
-1.047	-1.053	-0.981	-0.955	-0.888	-0.750	-0.509	-0.132	0.627	1.720	1.556	
-0.662	-0.594	-0.532	-0.534	-0.468	-0.295	-0.010	0.333	0.779	1.065		
-0.840	-0.775	-0.716	-0.725	-0.568	-0.412	-0.089	0.344	0.993	1.495		
-1.019	-0.955	-0.902	-0.917	-0.769	-0.572	-0.225	0.297	1.124	1.871		
-0.520	-0.561	-0.439	-0.390	-0.137	0.013	0.298	0.674	1.131	0.566		
-0.711	-0.657	-0.637	-0.574	-0.255	-0.055	0.310	0.867	1.547	1.015		
-0.903	-0.851	-0.836	-0.739	-0.416	-0.191	0.251	0.939	1.838	1.637		
-0.310	-0.296	-0.277	-0.131	0.058	0.268	0.673	1.008	0.602			
-0.497	-0.412	-0.416	-0.241	0.012	0.328	0.902	1.462	1.164			
-0.674	-0.591	-0.578	-0.386	-0.092	0.280	0.974	1.722	1.628			
-0.144	-0.013	0.050	0.197	0.476	0.629	0.968	0.586				
-0.314	-0.071	0.015	0.244	0.656	0.975	1.475	1.148				
-0.474	-0.220	-0.102	0.173	0.656	1.094	1.765	1.704				
0.333	0.405	0.576	0.683	0.914	0.868	0.494			P3		
0.345	0.553	0.797	1.079	1.462	1.514	1.123			P2		
0.283	0.516	0.809	1.187	1.677	1.899	1.656			P1		
1.014	1.032	1.198	1.055	0.507							
1.435	1.547	1.770	1.760	1.141							
1.571	1.730	2.024	2.129	1.678							
1.730	1.660	1.254									
1.792	1.872	1.254									
2.232	2.363	1.803									

Fig. 11. B&W core I 2-D pin power percent error distribution.

However, 64 pcm maximum eigenvalue difference was found at P2, and the lowest value of 5 pcm was found at P1 in the core critically problem (3B). An identical maximum pin power difference (2.10%) was observed with an average pin power difference of 0.791%–0.804%. The axial shape of the normalized power distribution is shown in Fig. 9, and the details of the percent pin power distribution error are shown in Fig. 10.

3.2.2. B&W simple experiments

The B&W [21] series 1484 core I and II 3-D problems were also analyzed. A detailed description of the benchmark problem is provided in Ref. [21], and the 2-D configuration of the core is shown in Fig. 2. However, the size of the core was still smaller than that of a conventional light water reactor. The total height of the core was 171.36 cm including 21.42 cm top and bottom water reflectors.

Table 8 summarizes the results of these analyses. The differences in the eigenvalues were relatively large compared to those of the 2-D problem (Tables 3 and 4). P1 shows a large difference in the eigenvalues and pin power distribution compared to P2 and P3 in both cases. On the other hand, core II shows a higher difference in both eigenvalues and pin power distribution compared to core I. the maximum pin power differences were 1.83%, 1.99%, and 2.48% at P3, P2, and P1, respectively, in core I and 4.46%, 4.46%, and 6.10% at P3, P2, and P1, respectively, in core II. The eigenvalue differences were 10965 pcm and 4802 pcm in cores I and II, respectively, at P0.

-0.644	-0.635	-0.588	-0.579	-0.610	-0.597	-0.530	-0.495	-0.569	-0.511	-0.498	-0.387	-0.352	-0.287	-0.264	-0.073	0.009	0.385	0.735	1.572	2.276	
-0.644	-0.635	-0.588	-0.579	-0.610	-0.597	-0.530	-0.495	-0.569	-0.511	-0.498	-0.387	-0.352	-0.287	-0.264	-0.073	0.009	0.397	0.735	1.572	2.262	
-0.808	-0.745	-0.698	-0.690	-0.724	-0.714	-0.649	-0.618	-0.633	-0.578	-0.567	-0.460	-0.352	-0.287	-0.264	-0.073	0.009	0.373	0.681	1.528	2.643	
-0.685	-0.750	-0.647	-0.536	-0.553	-0.568	-0.539	-0.516	-0.492	-0.443	-0.399	-0.381	-0.321	-0.265	-0.207	-0.140	0.077	0.357	0.833	1.595	2.238	
-0.685	-0.750	-0.647	-0.536	-0.610	-0.568	-0.539	-0.516	-0.492	-0.443	-0.399	-0.381	-0.321	-0.265	-0.207	-0.140	0.077	0.369	0.846	1.595	2.238	
-0.795	-0.805	-0.758	-0.648	-0.667	-0.684	-0.658	-0.639	-0.556	-0.510	-0.468	-0.381	-0.321	-0.265	-0.207	-0.041	0.098	0.369	0.819	1.595	2.692	
-0.756	-0.759	-0.576	-0.591	-0.614	-0.601	-0.584	-0.526	-0.433	-0.387	-0.343	-0.204	-0.356	-0.397	-0.230	-0.138	0.139	0.211	0.709	1.646	2.209	
-0.756	-0.759	-0.576	-0.591	-0.614	-0.601	-0.584	-0.588	-0.433	-0.387	-0.343	-0.278	-0.356	-0.397	-0.230	-0.138	0.139	0.223	0.723	1.646	2.209	
-0.866	-0.871	-0.688	-0.704	-0.729	-0.660	-0.644	-0.651	-0.497	-0.453	-0.413	-0.278	-0.435	-0.397	-0.230	-0.138	0.150	0.223	0.681	1.616	2.624	
-0.725	-0.615	-0.601	-0.666	-0.673	-0.501	-0.598	-0.491	-0.422	-0.374	-0.399	-0.456	-0.331	-0.158	-0.262	-0.011	0.051	0.322	0.862	1.737	2.167	
-0.725	-0.615	-0.601	-0.666	-0.673	-0.501	-0.598	-0.491	-0.422	-0.374	-0.399	-0.456	-0.331	-0.158	-0.262	-0.001	0.062	0.322	0.876	1.737	2.152	
-0.837	-0.784	-0.715	-0.780	-0.790	-0.620	-0.720	-0.617	-0.487	-0.442	-0.470	-0.531	-0.411	-0.243	-0.262	-0.001	0.073	0.347	0.848	1.706	2.558	
-0.661	-0.556	-0.508	-0.597	-0.655	-0.621	-0.580	-0.437	-0.501	-0.344	-0.466	-0.401	-0.367	-0.288	-0.274	-0.065	0.043	0.389	0.806	1.677	2.221	
-0.661	-0.614	-0.508	-0.597	-0.655	-0.621	-0.580	-0.437	-0.501	-0.413	-0.466	-0.401	-0.367	-0.288	-0.274	-0.065	0.043	0.389	0.806	1.677	2.221	
-0.775	-0.671	-0.623	-0.713	-0.774	-0.742	-0.704	-0.565	-0.567	-0.482	-0.466	-0.477	-0.448	-0.288	-0.274	-0.045	0.066	0.402	0.764	1.646	2.648	
-0.599	-0.599	-0.657	-0.484	-0.563	-0.545	-0.580	-0.474	-0.467	-0.475	-0.365	-0.414	-0.237	-0.410	-0.137	-0.102	0.126	0.441	0.887	1.722	2.412	
-0.599	-0.599	-0.657	-0.484	-0.563	-0.545	-0.580	-0.474	-0.467	-0.475	-0.365	-0.414	-0.237	-0.322	-0.137	-0.091	0.126	0.441	0.887	1.722	2.412	
-0.715	-0.715	-0.715	-0.603	-0.684	-0.607	-0.643	-0.540	-0.467	-0.546	-0.438	-0.414	-0.237	-0.322	-0.137	-0.049	0.161	0.467	0.887	1.737	2.877	
-0.593	-0.592	-0.552	-0.477	-0.442	-0.487	-0.448	-0.490	-0.553	-0.395	-0.242	-0.288	-0.263	-0.198	-0.066	0.011	0.071	0.288	0.823	1.481	2.326	
-0.593	-0.592	-0.552	-0.477	-0.442	-0.487	-0.448	-0.490	-0.553	-0.395	-0.242	-0.288	-0.263	-0.198	-0.066	0.011	0.071	0.288	0.838	1.481	2.310	
-0.712	-0.711	-0.672	-0.599	-0.566	-0.550	-0.513	-0.557	-0.622	-0.467	-0.317	-0.288	-0.348	-0.288	-0.066	0.032	0.094	0.302	0.808	1.465	2.726	
-0.425	-0.513	-0.519	-0.570	-0.466	-0.614	-0.456	-0.425	-0.507	-0.342	-0.331	-0.245	-0.312	-0.204	-0.168	0.024	0.277	0.428	0.895	1.595	2.232	
-0.425	-0.513	-0.581	-0.570	-0.466	-0.614	-0.456	-0.425	-0.507	-0.342	-0.331	-0.245	-0.312	-0.204	-0.168	0.024	0.290	0.428	0.911	1.611	2.232	
-0.548	-0.636	-0.643	-0.696	-0.594	-0.679	-0.590	-0.494	-0.578	-0.416	-0.409	-0.327	-0.312	-0.297	-0.168	0.057	0.314	0.442	0.895	1.595	2.646	
-0.427	-0.435	-0.499	-0.392	-0.468	-0.493	-0.437	-0.432	-0.360	-0.307	-0.323	-0.327	-0.250	-0.150	-0.224	0.001	0.186	0.487	0.725	1.559	2.396	
-0.427	-0.435	-0.499	-0.392	-0.468	-0.493	-0.437	-0.432	-0.360	-0.307	-0.323	-0.327	-0.250	-0.150	-0.224	0.001	0.199	0.501	0.741	1.559	2.396	
-0.491	-0.499	-0.563	-0.457	-0.534	-0.493	-0.507	-0.504	-0.360	-0.384	-0.403	-0.327	-0.250	-0.150	-0.182	0.081	0.262	0.544	0.757	1.593	2.905	
-0.476	-0.386	-0.466	-0.471	-0.450	-0.456	-0.522	-0.422	-0.429	-0.388	-0.398	-0.313	-0.198	-0.123	-0.136	0.145	0.248	0.326	0.901	1.570	2.253	
-0.476	-0.386	-0.466	-0.471	-0.519	-0.456	-0.522	-0.422	-0.429	-0.388	-0.398	-0.313	-0.198	-0.123	-0.136	0.145	0.261	0.326	0.901	1.588	2.253	
-0.542	-0.452	-0.533	-0.539	-0.588	-0.527	-0.594	-0.497	-0.506	-0.468	-0.398	-0.313	-0.198	-0.093	-0.093	0.204	0.314	0.400	0.918	1.624	2.750	
-0.470	-0.491	-0.420	-0.451	-0.328	-0.369	-0.393	-0.420	-0.346	-0.347	-0.334	-0.249	-0.084	-0.228	-0.035	0.169	0.166	0.347	0.973	1.827	2.444	
-0.470	-0.491	-0.420	-0.451	-0.328	-0.369	-0.393	-0.420	-0.346	-0.347	-0.334	-0.249	-0.084	-0.218	-0.035	0.182	0.180	0.362	0.973	1.827	2.444	
-0.539	-0.560	-0.490	-0.522	-0.400	-0.442	-0.469	-0.498	-0.427	-0.347	-0.334	-0.249	-0.084	-0.197	0.011	0.244	0.263	0.440	1.025	1.884	2.945	
-0.440	-0.385	-0.313	-0.291	-0.361	-0.282	-0.270	-0.319	-0.383	-0.434	-0.286	-0.317	-0.107	-0.129	0.101	0.029	0.252	0.367	1.115	1.968	2.548	
-0.440	-0.385	-0.387	-0.291	-0.361	-0.282	-0.270	-0.319	-0.383	-0.434	-0.286	-0.317	-0.107	-0.129	0.113	0.042	0.267	0.367	1.115	1.968	2.529	
-0.513	-0.459	-0.387	-0.366	-0.438	-0.282	-0.270	-0.401	-0.383	-0.434	-0.286	-0.317	-0.065	-0.074	0.173	0.134	0.354	0.465	1.187	2.047	3.077	
-0.399	-0.411	-0.359	-0.355	-0.337	-0.321	-0.271	-0.275	-0.368	-0.328	-0.109	-0.194	-0.161	-0.013	-0.063	0.200	0.345	0.449	1.094	2.026	2.329	
-0.399	-0.411	-0.359	-0.355	-0.337	-0.321	-0.271	-0.275	-0.368	-0.328	-0.109	-0.194	-0.161	-0.001	-0.063	0.214	0.345	0.449	1.094	2.026	2.329	
-0.399	-0.411	-0.438	-0.435	-0.418	-0.321	-0.356	-0.275	-0.368	-0.328	-0.109	-0.142	-0.084	0.070	0.040	0.354	0.484	0.570	1.210	2.152	2.931	
-0.246	-0.308	-0.303	-0.292	-0.399	-0.308	-0.122	-0.154	-0.212	-0.176	-0.164	-0.122	-0.158	0.028	0.192	0.277	0.367	0.750	1.244	1.930	2.654	
-0.246	-0.308	-0.303	-0.292	-0.399	-0.219	-0.122	-0.154	-0.212	-0.176	-0.153	-0.122	-0.146	0.028	0.206	0.292	0.367	0.768	1.265	1.952	2.654	
-0.330	-0.392	-0.303	-0.377	-0.399	-0.308	-0.213	-0.247	-0.212	-0.166	-0.143	-0.078	-0.087	0.092	0.288	0.411	0.499	0.898	1.369	2.065	3.233	
-0.271	-0.197	-0.383	-0.198	-0.215	-0.219	-0.132	-0.199	-0.084	-0.169	-0.069	0.023	0.046	-0.057	0.172	0.289	0.562	0.792	1.010	2.022	2.739	
-0.271	-0.197	-0.383	-0.198	-0.215	-0.219	-0.132	-0.199	-0.084	-0.169	-0.069	0.035	0.046	-0.044	0.187	0.305	0.580	0.812	1.010	2.022	2.739	
-0.271	-0.197	-0.383	-0.198	-0.215	-0.219	-0.132	-0.210	-0.063	-0.147	-0.035	0.083	0.135	0.038	0.291	0.451	0.741	0.972	1.168	2.192	3.364	
-0.186	-0.118	-0.114	-0.150	-0.055	-0.145	-0.102	-0.112	-0.027	-0.026	0.122	0.154	0.189	0.162	0.280	0.403	0.496	0.734	1.265	2.088	2.629	
-0.186	-0.118	-0.114	-0.139	-0.055	-0.135	-0.102	-0.112	-0.027	-0.026	0.134	0.167	0.202	0.177	0.296	0.420	0.516	0.734	1.290	2.115	2.629	
-0.186	-0.118	-0.114	-0.139	-0.034	-0.103	-0.069	-0.068	0.042	0.033	0.196	0.259	0.328	0.311	0.458	0.615	0.711	0.952	1.486	2.354	3.389	
-0.061	0.025	0.124	-0.021	0.094	0.052	0.085	0.235	0.109	0.169	0.187	0.370	0.271	0.290	0.511	0.547	0.763	1.034	1.719	2.332	2.929	
-0.061	0.025	0.124	-0.010	0.094	0.052	0.085	0.248	0.121	0.182	0.201	0.385	0.271	0.290	0.529	0.567	0.784	1.058	1.719	2.361	2.929	
-0.061	0.036	0.124	0.001	0.105	0.075	0.108	0.272	0.172	0.235	0.284	0.472	0.394	0.439	0.690	0.762	1.000	1.299	1.962	2.655	3.739	
0.299	0.227	0.323	0.308	0.354	0.333	0.410	0.298	0.403	0.509	0.399	0.718	0.658	0.743	1.041	0.843	0.984	1.259	1.735	2.563	2.885	
0.311	0.227	0.335	0.320	0.354	0.333	0.410	0.298	0.418	0.509	0.415	0.718	0.658	0.761	1.061	0.843	1.008	1.286	1.735	2.563	2.885	
0.287	0.215	0.323	0.320	0.354	0.346	0.424	0.312	0.446	0.568	0.492	0.815	0.778	0.891	1.220	1.039	1.250	1.556	2.007	2.891	3.762	
0.738	0.773	0.784	0.756	0.824	0.915	0.623	0.813	0.817	0.964	0.835	1.136	1.189	1.190	1.439	1.462	1.480	1.988	2.332	3.002	3.339	
0.738	0.773	0.798	0.770	0.824	0.915	0.638	0.828	0.833	0.964	0.835	1.136	1.189	1.210	1.439	1.486	1.480	1.988	2.366	3.002	3.339	
0.684	0.718	0.729	0.714	0.767	0.886	0.608	0.813	0.833	0.980	0.870	1.190	1.286	1.314	1.573	1.657	1.697	2.260	2.636	3.408	4.327	
1.641	1.617	1.685	1.813	1.734	1.582	1.555	1.588	1.730	1.619	1.764	1.977	1.877	1.994	2.087	2.008	2.566	2.570	3.113	3.629	3.944	P3
1.641	1.617	1.685	1.813	1.734	1.582	1.555	1.588	1.730	1.637	1.764	1.977	1.877	2.017	2.087	2.034	2.595	2.570	3.150	3.629	3.944	P2
1.582	1.572	1.625	1.752	1.687	1.566	1.523	1.555	1.730	1.637	1.802	2.036	1.982	2.130	2.257	2.247	2.859	2.898	3.518	4.194	5.198	P1
2.299	2.203	2.291	2.453	2.333	2.156	2.281	2.269	2.317	2.335	2.422	2.486	2.594	2.658	2.723	2.775	2.728	3.320	3.610	3.846	4.466	
2.284	2.203	2.291	2.439	2.318	2.156	2.266	2.269	2.317	2.335	2.422	2.486	2.594	2.658	2.723	2.775	2.728	3.320	3.610	3.846	4.466	
2.539	2.516	2.578	2.728	2.627	2.487	2.559	2.571	2.679	2.695	2.799	2.902	3.056	3.108	3.233	3.408	3.429	4.101	4.491	4.985	6.103	

Fig. 12. B&W core II 2-D fuel pin power percent error distribution (Octant).

Table 9
Computing time of the 2-D and 3-D numerical problems.

Problem	PN order	Number of Threads (mins)		
		1	8	16
1484 core I (2-D)	P3	10.61	3.65	4.53
	P2	8.46	3.60	4.15
	P1	6.81	3.36	3.86
	TCP0	2.11	0.37	0.25
3A (3-D)	P3	206.40	28.06	14.80
	P2	165.00	22.76	11.36
	P1	121.80	16.59	8.97
	TCP0	68.40	9.18	5.17

The detailed pin power differences of cores I and II are shows in Figs. 11 and 12, respectively.

4. Parallelization

To study the acceleration of parallelization, different numbers n of threads (n = 1, 8,16) were used to execute the numerical problem. Table 9 shows the execution time versus the number of threads. This shows that, as the number of threads increases, the acceleration factor increases almost linearly in the case of the 3-D problem. In 2-D, the execution time increases when 16 threads are used owing to the small numerical problem. However, the performance of the transport-corrected (TCP0) problem is faster than that of the higher order (two to three times that of P1). In conclusion, further simulations and code development are required to reduce the computing time.

5. Conclusions

The MOC using a higher-order scattering source yields comparatively accurate results. Most of the improvement results from the first order (P1), but increasing the number of scattering sources leads to a smaller error, except for 3B. There was no significant bias observed in different geometries with the presence of a reflector or baffle, number of Gd pins, number of control rods (AIC and B4C), and boron concentration. Less than 100 pcm eigenvalue differences with not more than 1% maximum pin power difference were observed in most of the problems. However, in the lattice analysis, the eigenvalue difference was slightly higher with a change in temperature, but this change is not significant. On the other hand, the calculated control rod worth completely matched (<10 pcm) the reference. In the case of large quarter-core 2-D problem, the average assembly power distribution errors of uncontrolled core (no control rods were used) were 0.912%, 0.924%, and 0.598% at P3, P2, and P1, respectively. Whereas the average assembly power distribution errors of controlled core (AIC control rods were used) were 0.450%, 0.453%, and 0.443% at P3, P2, and P1, respectively and 0.492%, 0.492%, and 0.493% at P3, P2, and P1, respectively when B4C control rods were used. A similar trend was found in the 3-D problems, except for B&W core II. A higher pin power (4.46% maximum pin power) was recorded on the peripheral pin (low power) of the core as a result of the rectangular arrangement of the core. We believe that this work makes a valuable contribution to the verification of the methods used in STREAM.

Declaration of competing interest

The authors declare that they have no known competing financial interests or personal relationships that could have appeared to influence the work reported in this paper.

Acknowledgements

This work was supported by a National Research Foundation of Korea (NRF) grant funded by the Korean government (MSIT). (No. NRF-2019M2D2A1A03058371).

References

[1] S. Choi, D. Lee, “Three-dimensional method of characteristics/diamond-difference transport analysis method in STREAM for whole-core neutron transport calculation”. Comput. Phys. Commun., 260, 107332. https://doi.org/10.1016/j.cpc.2020.107332.
[2] D. Knott, A. Yamamoto, Lattice physics computations, Handbook of Nuclear Engineering (2010) 913–1239.
[3] X-5 Monte Carlo Team, “MCNP - A General N-Particle Transport Code, Version 5” Volume I: Overview and Theory, U. R.-03-1987, 2003. updated 2005.
[4] H. Lee, W. Kim, P. Zhang, M. Lemaire, A. Khassenov, J. Yu, Y. Jo, J. Park, D. Lee, “MCS - a Monte Carlo particle transport code for large-scale power reactor analysis,” Ann. Nucl. Energy, 139, 107276. https://doi.org/10.1016/j.anucene.2019.107276.
[5] S. Choi, K. Smith, H.C. Lee, D. Lee, Impact of inflow transport approximation on light water reactor analysis, Comp. Physiol. 299 (2015) 352–373, https://doi.org/10.1016/j.jcp.2015.07.005.
[6] M.J. Halsall, CACTUS, A Characteristic Solution to the Neutron Transport Equation in Complicated Geometries, AEEW-R, UK Atomic Energy Authority Establishment, Winfrith, 1980.
[7] H.G. Joo, J.Y. Cho, K.-S. Kim, C.C. Lee, S.Q. Zee, Methods and performance of a three-dimensional whole-core transport code DeCART, in: Proceedings of PHYSOR 2004, 2004. Chicago, IL.
[8] Y.S. Jung, C.B. Shim, C.H. Lim, H.G. Joo, Practical numerical reactor employing direct whole core neutron transport and subchannel thermal/hydraulic solvers, Ann. Nucl. Energy 62 (2015) 357–374, https://doi.org/10.1016/j.anucene.2013.06.031.
[9] B. Collins, S. Stimpson, B. Kochunas, T. Downar, Assessment of the 2D/1D implementation in MPACT, in: Proceedings of PHYSOR 2014, Sep. 29, 2014. Kyoto, Japan.
[10] A. Marin-Lafleche, M.A. Smith, C.H. Lee, PROTEUS-MOC: a 3D deterministic solver incorporating 2D method of characteristics, in: Proceedings of M&C 2013, 2013. Sun Valley.
[11] W. Boyd, S. Shaner, L. Li, B. Forget, K. Smith, The OpenMOC method of characteristics neutral particle transport code, Ann. Nucl. Energy 68 (2014) 43–52, https://doi.org/10.1016/j.anucene.2013.12.012.
[12] M. Jarrett, B. Kochunas, E. Larsen, T. Downar, Progress in characterizing 2D/1D accuracy in MPACT, in: Proceedings of M&C 2017, 2017. Jeju, South Korea.
[13] A.M. Graham, B.S. Collins, T. Downar, Improvement of the 2D/1D method in MPACT using the subplane scheme, in: Proceedings of M&C 2017, 2017. Jeju, South Korea.
[14] Z. Liu, H. Wu, L. Cao, Q. Chen, Y. Li, A new three-dimensional method of characteristics for the neutron transport calculation, Ann. Nucl. Energy 38 (2011) 447–454, https://doi.org/10.1016/j.anucene.2010.09.021.
[15] M.A. Shafii, Solution methods of neutron transport equation in nuclear reactors, J. I. Dasar 14 (2013) 59–65, https://doi.org/10.19184/jid.v14i2.320.
[16] Liangzhi Cao, Hongchun Wu, Spherical harmonics method for neutron transport equation based on unstructured-meshes, Nucl. Sci. Tech. 15 (2004).
[17] K. Kobayashi, H. Oigawa, H. Yamagata, The spherical harmonics method for the multigroup transport equation in x-y geometry, Ann. Nucl. Energy 13 (1986) 663–678, https://doi.org/10.1016/0306-4549(86)90045-9.
[18] A. Rahman, A. Cherezov, D. Lee, Higher Order PN Solver in Method of Characteristics Code STREAM, Transactions of the Korean Nuclear Society Autumn Meeting Changwon, Korea, 2020.
[19] G. Palmiotti, E. E. Lewis, C. B. Carrico, VARIANT: VARIational Anisotropic Nodal Transport for Multidimensional Cartesian and Hexagonal Geometry Calculation, ANL-95/40, Argonne National Laboratory, USA.
[20] A.T. Godfrey, Vera Core Physics Benchmark Progression Problem Specifications, Fourth Revision, CASL, 2014. CASL-U-2012-0131-004.
[21] M.N. Baldwin, G.S. Hoovler, R.L. Eng, F.G. Welfare, Critical Experiments Supporting Close Proximity Water Storage of Power Reactor Fuel, The Babcock & Wilcox Company, 1979.